Research Square

Preprints are preliminary reports that have not undergone peer review.
They should not be considered conclusive, used to inform clinical practice,
or referenced by the media as validated information.

AI powered Structural Health Monitoring via Piezoelectric Sensors

Akash M A

aakashaanand@protonmail.com

M S Ramaiah University of Applied Sciences

Research Article

Keywords: Structural health monitoring, piezoelectric transducers, finite element analysis, support vector machine, Gaussian process regression.

Posted Date: November 17th, 2026

DOI: https://doi.org/10.21203/rs.3.rs-11734968/v1

License: This work is licensed under a Creative Commons Attribution 4.0 International License.
Read Full License

Additional Declarations: The authors declare no competing interests.

AI-powered Structural Health Monitoring via Piezoelectric Sensors

Akash Mandur Anand

M S Ramaiah University of Applied Sciences Peenya 4th Phase, Peenya, Bengaluru, Karnataka 560058

Corresponding author email: aakashaanand@protonmail.com

Abstract

Accurate and cost-effective detection and localization of structural damage are important goals in structural health monitoring (SHM), particularly for lightweight metallic structures that are vulnerable to fatigue cracks. Such cracks can reduce the strength and reliability of a structure before they are identified through conventional inspection methods. In this study, an finite-element FEM and machine learning-based approach is proposed for detecting and locating cracks in an aluminum beam using a surface-mounted piezoelectric (PZT) actuator and sensor.

A parametric finite element analysis was carried out using COMSOL Multiphysics, where a rectangular crack was progressively moved along the beam from 20 to 180 mm in 5 mm increments. The resulting floating electric potential was recorded at the four measurement points under transient conditions, producing more than 500 time-series responses. Two additional multi-crack configurations were also modeled to examine more complex damage scenarios, although these configurations were not included in the machine-learning dataset.

From each transient response, six features were extracted at each measurement point: root-mean-square amplitude, peak amplitude, peak-to-peak amplitude, kurtosis, Hilbert-envelope arrival time, and dominant frequency. This resulted in a 24-dimensional feature vector for each response.

A support vector machine (SVM) classifier was then trained to distinguish between healthy and cracked beam conditions. Grid search was used to select the most suitable kernel from linear and radial basis function (RBF) options. For crack localization, a Gaussian process regression (GPR) model with a Matèrn covariance kernel was trained using only the cracked-state data. The model achieved a mean absolute error of 25.09 mm and provided 95% prediction confidence intervals.

Principal component analysis (PCA) was also used to visualize the distribution of the cracked-state features. In addition, the trained SVM classifier was applied sequentially along a simulated monitoring timeline to demonstrate how the probability of damage could evolve over time.

However, the results should be interpreted as a proof of concept rather than as a validated damage-detection accuracy. In particular, the healthy-state data were synthetically generated by augmenting a single cracked-beam simulation instead of being obtained from an independent healthy-beam simulation. The study demonstrates the potential of combining piezoelectric sensing, FEM simulations, and machine learning for structural damage detection and crack localization.

Keywords

Structural health monitoring, piezoelectric transducers, finite element analysis, support vector machine, Gaussian process regression.

1. Introduction

A. Structural Health Monitoring

Structural Health Monitoring (SHM) is an important approach for detecting and assessing damage in engineering structures. It generally involves the use of permanently installed or periodically deployed sensors to identify the presence, location, and extent of structural damage before it develops into a serious failure .

For metallic structures, conventional inspection methods include visual inspection, ultrasonic testing, and other non-destructive testing (NDT) techniques. Although these methods are widely used, they can be time-consuming and may require the structure or equipment to be taken out of service during inspection . In addition, some internal or early-stage defects may be difficult to identify through visual inspection alone. These limitations have increased interest in sensor-based SHM techniques that can provide continuous or periodic information about the structural condition.

B. Piezoelectric Materials for Structural Health Monitoring

Piezoelectric materials, particularly lead zirconate titanate (PZT), are widely used in SHM because of their ability to convert mechanical and electrical energy into one another . When 7mechanical stress is applied to a piezoelectric material, it generates an electrical response, which is known as the direct piezoelectric effect. Conversely, applying an electric field causes mechanical deformation, referred to as the converse piezoelectric effect.

This reversible electromechanical behavior allows PZT elements to perform both sensing and actuation functions. As an actuator, a PZT patch can receive an electrical excitation and introduce mechanical vibrations into the host structure. As a sensor, it can detect the resulting structural response and convert it into an electrical signal.

PZT elements are particularly attractive for SHM because they are relatively small, lightweight, and can be directly attached to the surface of a structure . Their ability to operate as both actuators and sensors makes them useful for detecting changes in structural behavior caused by defects such as cracks .

C. Transient Responses and Crack Detection

When a PZT actuator applies an excitation to a thin structural component such as a beam or plate, the resulting mechanical disturbance propagates through the structure. If the structure contains a discontinuity, such as a crack, hole, or change in cross-section, the propagating response can be altered. A crack can change the local stiffness and affect the propagation of the mechanical response through phenomena such as reflection, scattering, or mode conversion. As a result, a receiving PZT sensor may record a response that differs from that of an undamaged structure. These changes can appear in measurable characteristics such as signal amplitude, arrival time, or frequency content.

In this study, the response is described as the transient electromechanical response of the beam, specifically the floating electric potential measured at selected points. Although the excitation produces a propagating mechanical response, the present numerical model does not explicitly establish a particular guided-wave mode, such as the S0 or A0 Lamb wave modes. Furthermore, the excitation waveform used to generate the transient dataset is not sufficiently documented to justify assigning the response to a specific guided-wave mode. Therefore, a general description of the transient electromechanical response is used throughout this work.

D. Machine Learning for Structural Health Monitoring

Machine learning (ML) has increasingly been investigated as a tool for structural health monitoring because of its ability to identify patterns in large amounts of sensor data. Different ML techniques can be used depending on the monitoring objective. Classification methods can determine whether a structure is damaged, while regression methods can estimate parameters such as damage location or severity. Dimensionality-reduction techniques can also be used to visualize complex feature spaces and identify patterns within the collected data.

In this study, Support Vector Machine (SVM), Principal Component Analysis (PCA), and Gaussian Process Regression (GPR) are used for different purposes. SVM is a supervised learning method that determines a decision boundary between different classes. Kernel functions, such as the linear and radial basis function (RBF) kernels, can be used to model both linear and nonlinear relationships in the data.

PCA is used as a dimensionality-reduction and visualization technique . It transforms a high-dimensional feature space into a smaller number of orthogonal components that capture the largest amount of variation in the data. In this work, PCA is used primarily to visualize the distribution of the extracted features rather than as a damage classifier.

GPR provides a probabilistic approach to regression . Unlike methods that provide only a single predicted value, GPR produces a predictive distribution, allowing the uncertainty associated with the prediction to be estimated. This is particularly useful in SHM, where knowing the confidence of a predicted crack location can be as important as the predicted location itself.

Previous studies have also shown that incorporating physical information into the mean and covariance functions of GPR can improve prediction accuracy and extrapolation performance.

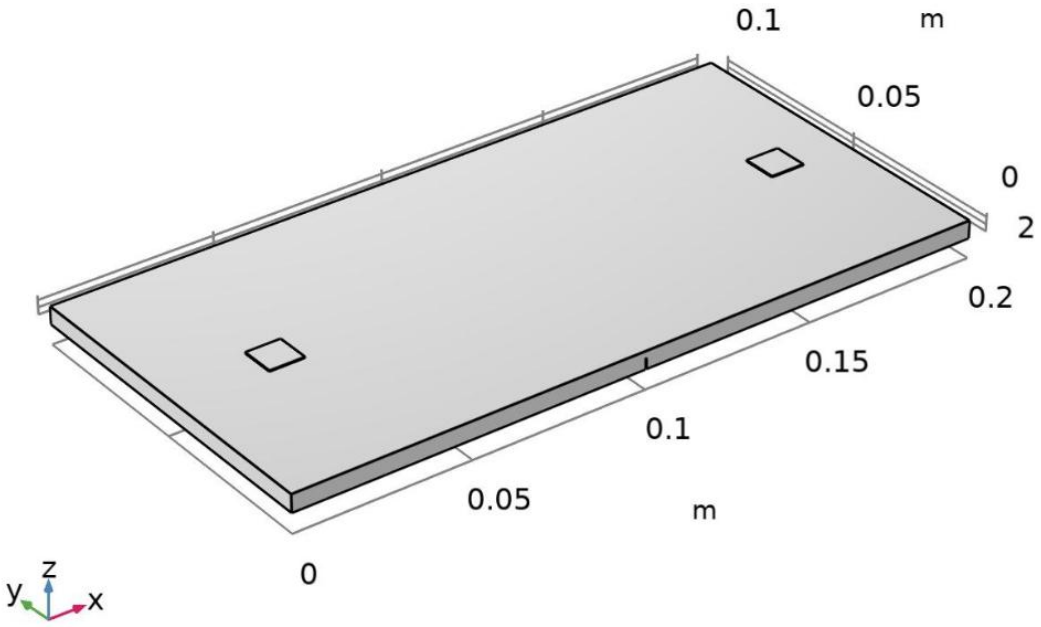
Other studies have explored constrained and structured GPR approaches for crack and defect localization, particularly when dealing with sparse measurements and boundary-related effects.

2. Mathematical Formulation

A. Geometry and Coordinate System

A Cartesian coordinate system (x, y, z) is defined with its origin at one corner of the beam, consistent with the COMSOL model geometry. The aluminium beam has a length L=200mm, width b=100, and thickness h= 5 mm, corresponding to the x, y, and z directions, respectively.

A PZT actuator with dimensions 10 × 10 × 0.3 mm is bonded to the top surface of the beam



at (25,45,5) mm. An identical PZT sensor is positioned at (175,45,5) mm.

Figure 1: Beam geometry, piezoelectric actuator and sensor layout, generated in COMSOL Multiphysics.

B. Mechanical Governing Equations

The mechanical behaviour of the aluminium beam is described using the elastodynamic equilibrium equation:

$$\nabla \cdot \sigma + f = \rho \ddot{u} \qquad 1$$

Where σ represents the Cauchy stress tensor, f is the applied body force per unit volume, ρ is the material density, and ¨ represents the acceleration of the displacement field u (x,y,z,t).

In the present model, no external body force is assumed unless otherwise specified. The mechanical excitation is introduced through the appropriate boundary conditions of the model rather than through the body-force term.

Strain-Displacement Relationship

Since the FEM model assumes small deformations, the strain in the aluminum beam can be related to the displacement field using the linear strain-displacement relationship:

$$\varepsilon = \tfrac{1}{2}(\nabla u + (\nabla u)^T) \qquad 2$$

Where ε is the strain tensor, and u is the displacement field.

This relationship assumes that the deformation of the beam is sufficiently small that nonlinear geometric effects can be neglected, which is consistent with the linear elastic formulation used in the numerical model.

C. Crack Representation

Cracks are directly introduced to the finite element geometry as rectangular slots in the aluminum beam with defined length or width, opening, depth, and position.

Four crack configurations are defined on the provided COMSOL geometry. The first crack configuration was used as the parameter for the parametric sweep, while the other three were used as fixed geometries and excluded from the machine-learning dataset.

Table 1

Crack	Width (mm)	Depth (mm)	Height (mm)	Position (x,y,z)
Crack 1	62.45	1.93	3	x = 20-180 (swept, 5 mm step), y = 45, z = 0
Crack 2	77	2.09	3	(110,30,0)
Crack 3	67.5	2.16	3	(90,90,0)
Crack 4	37.47	2.22	3	(30,10,0)

For Crack 1, the position is varied along the x-direction from 20 to 180 mm in 5 mm increments, allowing the influence of crack location on the beam's electromechanical response to be

investigated.

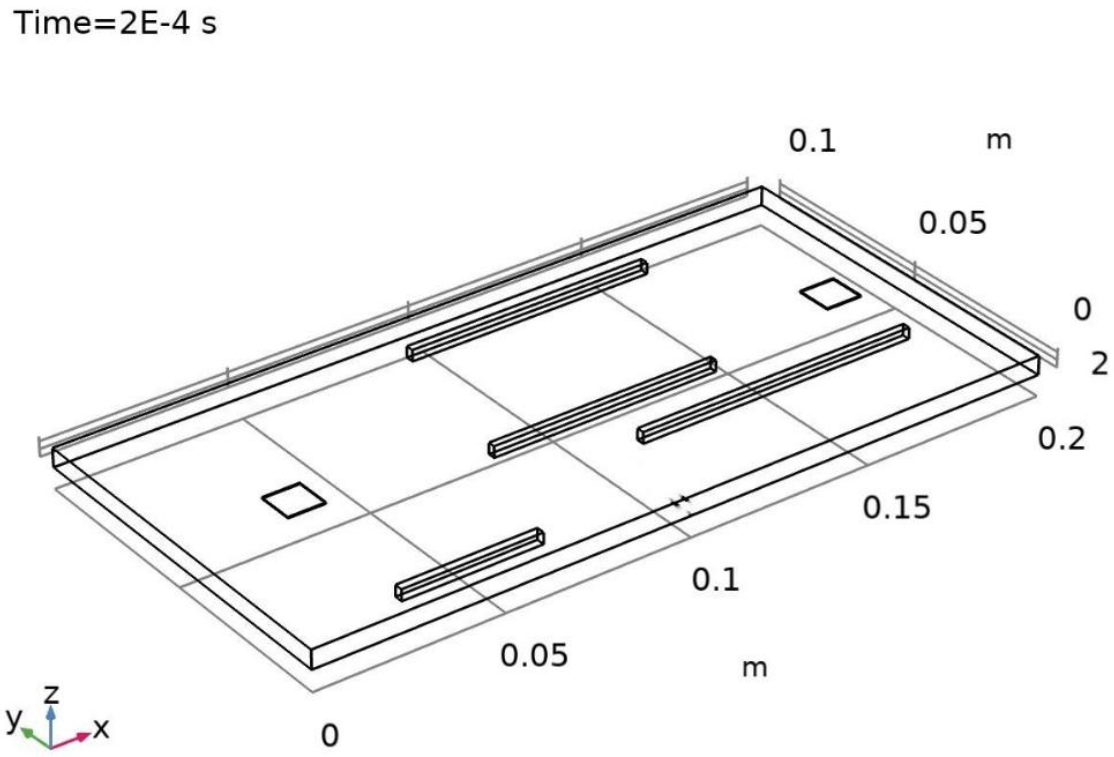


Figure 2 : The four confirmed crack configurations and the piezoelectric actuator/sensor layout, shown together on the beam geometry

3. FEM Simulation and Dataset Generation

A. FEM Model and Simulation Setup

The finite-element model was developed in COMSOL Multiphysics to study the response of an aluminum beam with surface-bonded piezoelectric elements. The beam was modelled with dimensions of 200 x 100 x 5 mm. A piezoelectric actuator and sensor, each measuring 10 x 10 x 0.3 mm, were placed on the beam surface. The actuator was positioned at 25,45,5 mm, and the sensor was positioned at 175,45,5 mm.

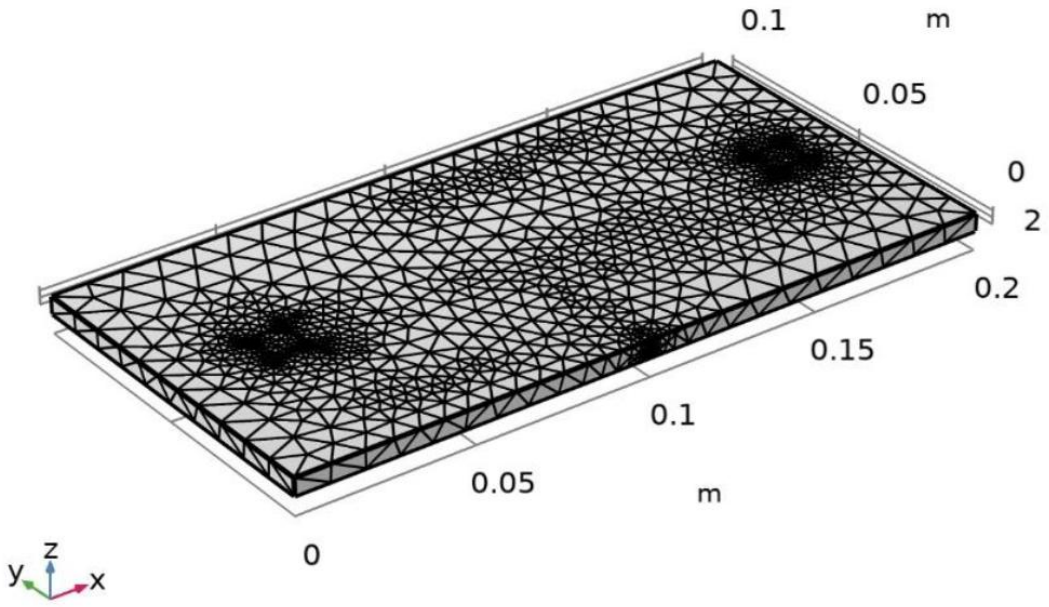
The structural and piezoelectric behaviors were modelled by coupling the Solid Mechanics and electrostatics physics interfaces. An electrical excitation was applied to the actuator, which produced a mechanical response in the beam. The response was then captured through the floating electric potential obtained at the selected measurement points.

The beam, piezoelectric elements, and crack geometries were discretized using a finite-element mesh. Local refinement was applied around the piezoelectric elements and crack regions to represent the structural response more effectively. Frequency-domain and transient studies were carried out in COMSOL. The frequency-domain analysis was performed over the

frequency range of 50–350 Hz, while the transient analysis was used to obtain the time-dependent response for different crack positions.

The simulation outputs were exported in CSV format. Each file contained a time column along with the corresponding floating electric potential values. The responses obtained at

measurement Points 14, 16, 22, 24 and so on were used for further signal processing, feature



extraction, and machine-learning analysis.

Figure 3: Finite Element Mesh discretization showing refinement across the structural domain.

B. Crack Cases and Dataset Generation

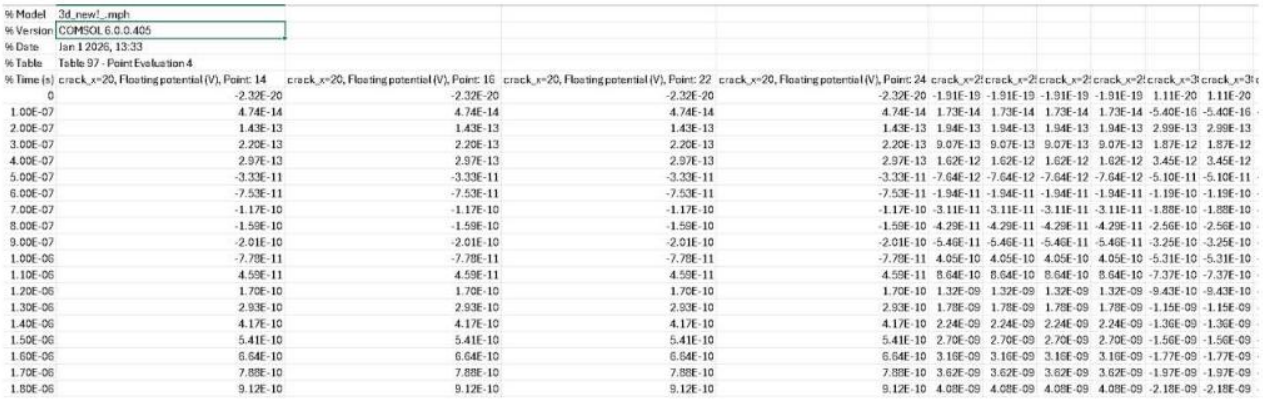
Crack 1 was selected as the main crack configuration for generating the dataset. Its position along the -axis varied from 20 to 180 mm in steps of 5 mm, resulting in different crack positions. The dimensions of Crack 1 were kept constant at 62.45 x 1.93 x 3 mm.

For each crack position, a transient simulation was performed in COMSOL. The floating electric potential was recorded at measurement Points 14, 16, 22, 24, and so on and the corresponding time-domain signals were exported in CSV format. The transient simulation used a time step of 1×10^{-7}s.

The exported CSV dataset consisted of a time column and several response columns corresponding to different crack positions and measurement points. The crack position was represented in the column headings using the parameter crack_x. For example, a column containing crack_x=20 represents the floating-potential response obtained when Crack 1 was located at $x = 20$mm.

The dataset was generated through the following process: the crack position was first defined in the COMSOL model, followed by the transient simulation and extraction of the floating-potential responses. This process was repeated for all 33 Crack 1 positions. The exported signals were then organized and prepared for feature extraction and machine-learning analysis.

Crack 2 and Crack 3 were also considered as additional crack configurations. Crack 2 was located at $= 110$mm and had dimensions of 77 x 2.09 x 3 mm, while Crack 3 was located at $x = 90$mm and had dimensions of 67.5 x 2.16 x 3 mm. These cases were used as supplementary crack configurations and were not included as the primary parametric samples for machine-learning model development.



% Model	3d_new!_.mph										
% Version	COMSOL 6.0.0.405										
% Date	Jan 1 2026, 13:33										
% Table	Table 97 - Point Evaluation 4										
% Time (s)	crack_x=20, Floating potential (V), Point: 14	crack_x=20, Floating potential (V), Point: 16	crack_x=20, Floating potential (V), Point: 22	crack_x=20, Floating potential (V), Point: 24	crack_x=2	crack_x=2	crack_x=2	crack_x=2	crack_x=3	crack_x=3	
0	-2.32E-20	-2.32E-20	-2.32E-20	-2.32E-20	-1.91E-19	-1.91E-19	-1.91E-19	-1.91E-19	1.11E-20	1.11E-20	
1.00E-07	4.74E-14	4.74E-14	4.74E-14	4.74E-14	1.73E-14	1.73E-14	1.73E-14	1.73E-14	-5.40E-16	-5.40E-16	
2.00E-07	1.43E-13	1.43E-13	1.43E-13	1.43E-13	1.94E-13	1.94E-13	1.94E-13	1.94E-13	2.99E-13	2.99E-13	
3.00E-07	2.20E-13	2.20E-13	2.20E-13	2.20E-13	9.07E-13	9.07E-13	9.07E-13	9.07E-13	1.87E-12	1.87E-12	
4.00E-07	2.97E-13	2.97E-13	2.97E-13	2.97E-13	1.62E-12	1.62E-12	1.62E-12	1.62E-12	3.45E-12	3.45E-12	
5.00E-07	-3.33E-11	-3.33E-11	-3.33E-11	-3.33E-11	-7.64E-12	-7.64E-12	-7.64E-12	-7.64E-12	-5.10E-11	-5.10E-11	
6.00E-07	-7.53E-11	-7.53E-11	-7.53E-11	-7.53E-11	-1.94E-11	-1.94E-11	-1.94E-11	-1.94E-11	-1.19E-10	-1.19E-10	
7.00E-07	-1.17E-10	-1.17E-10	-1.17E-10	-1.17E-10	-3.11E-11	-3.11E-11	-3.11E-11	-3.11E-11	-1.88E-10	-1.88E-10	
8.00E-07	-1.59E-10	-1.59E-10	-1.59E-10	-1.59E-10	-4.29E-11	-4.29E-11	-4.29E-11	-4.29E-11	-2.56E-10	-2.56E-10	
9.00E-07	-2.01E-10	-2.01E-10	-2.01E-10	-2.01E-10	-5.46E-11	-5.46E-11	-5.46E-11	-5.46E-11	-3.25E-10	-3.25E-10	
1.00E-06	-7.78E-11	-7.78E-11	-7.78E-11	-7.78E-11	4.05E-10	4.05E-10	4.05E-10	4.05E-10	-5.31E-10	-5.31E-10	
1.10E-06	4.59E-11	4.59E-11	4.59E-11	4.59E-11	8.64E-10	8.64E-10	8.64E-10	8.64E-10	-7.37E-10	-7.37E-10	
1.20E-06	1.70E-10	1.70E-10	1.70E-10	1.70E-10	1.32E-09	1.32E-09	1.32E-09	1.32E-09	-9.43E-10	-9.43E-10	
1.30E-06	2.93E-10	2.93E-10	2.93E-10	2.93E-10	1.78E-09	1.78E-09	1.78E-09	1.78E-09	-1.15E-09	-1.15E-09	
1.40E-06	4.17E-10	4.17E-10	4.17E-10	4.17E-10	2.24E-09	2.24E-09	2.24E-09	2.24E-09	-1.36E-09	-1.36E-09	
1.50E-06	5.41E-10	5.41E-10	5.41E-10	5.41E-10	2.70E-09	2.70E-09	2.70E-09	2.70E-09	-1.56E-09	-1.56E-09	
1.60E-06	6.64E-10	6.64E-10	6.64E-10	6.64E-10	3.16E-09	3.16E-09	3.16E-09	3.16E-09	-1.77E-09	-1.77E-09	
1.70E-06	7.88E-10	7.88E-10	7.88E-10	7.88E-10	3.62E-09	3.62E-09	3.62E-09	3.62E-09	-1.97E-09	-1.97E-09	
1.80E-06	9.12E-10	9.12E-10	9.12E-10	9.12E-10	4.08E-09	4.08E-09	4.08E-09	4.08E-09	-2.18E-09	-2.18E-09	

Figure 4 : Representation of the extracted physics-guided dataset compiling statistical features across varied dynamic damage scenarios.

4. Signal Processing and Feature Extraction

Each FEM simulation generated a time-dependent floating electric potential response at measurement Points 14, 16, 22, 24 and so on. The simulation results were exported from COMSOL in CSV format, with the time values and corresponding potential responses arranged in separate columns. These signals were used to study how changes in crack position affected the measured response.

The raw signals were used directly for feature extraction without applying additional filtering or normalization. For the synthetically generated healthy-class data, circular time shifting, random amplitude scaling, and additive Gaussian noise were applied to the reference signal, as explained in Section 3.2. After feature extraction, the resulting features were standardized before being supplied to the machine-learning models.

Six features were extracted from the signal at each measurement point. Four of these were time-domain features: peak amplitude, peak-to-peak amplitude, root mean square (RMS), and kurtosis. The peak amplitude represents the maximum absolute value of the signal and was calculated as:

$$A_{peak} = max/x_i/ \qquad 3$$

The peak-to-peak amplitude was obtained from the difference between the maximum and minimum signal values:

$$A_{p-p} = max(x_i) - min(x_i) \qquad 4$$

The RMS value was calculated to describe the overall magnitude of the signal:

$$x_{RMS} = \sqrt{\frac{1}{N}\sum_{i=1}^{N} x_i^2} \qquad 5$$

Kurtosis was calculated to describe the distribution and impulsive characteristics of the signal:

$$K = \frac{\frac{1}{N}\sum_{i=1}^{N}(x_i - \hat{x})^4}{[\frac{1}{N}\sum_{i=1}^{N}(x_i - \hat{x})^2]^2} \qquad 6$$

where represents the signal value at the i-th sample, is the total number of samples, and x^is the mean of the signal.

Frequency-domain information was obtained using the Fast Fourier Transform (FFT). The dominant frequency was identified as the frequency corresponding to the maximum magnitude of the Fourier spectrum:

$$f_{peak} = \underset{f}{argmax}/X(f)/ \qquad 7$$

where X(f)is the Fourier transform of the signal.

A Hilbert-transform-based envelope was also calculated to estimate the signal arrival time.

The envelope was obtained using:

$$e(t) = /Hilbert[x(t)]/ \qquad 8$$

The first time at which the envelope exceeded a threshold equal to 2.5 times its RMS value was taken as the time of flight (ToF):

$$ToF = min\{t: e(t) > 2.5 \times RMS[e(t)]\} \qquad 9$$

If the envelope did not cross the threshold, the ToF value was assigned as zero. This method provided a simple way to estimate the arrival of the main signal response.

The features from the four measurement points got combined into a 24 dimensional vector. Standardization came before training to keep different scales from affecting the models too much. The machine learning process had two main tasks which were crack detection and crack localization.

5. Machine-Learning Methodology

The features from the four measurement points got combined into a 24 dimensional vector. Standardization came before training to keep different scales from affecting the models too much.

The machine learning process had two main tasks which were crack detection and crack localization. For crack detection, a Support Vector Machine (SVM) was used to classify the beam condition as either healthy or cracked. Both linear and radial basis function (RBF) kernels were considered. The regularization parameter was selected from the values 0.1, 1, 10, and 100. Grid search with three-fold cross-validation was used to identify the best combination of parameters. The dataset consisted of 68 samples, including 33 cracked samples and 35 synthetically generated healthy samples. An 80:20 training and testing split was used, with the random seed set to 42.

Gaussian Process Regression (GPR) was used to estimate the crack location. The model was trained using the 33 cracked samples, with the extracted signal features as inputs and the longitudinal position of Crack 1 as the target. A Matèrn kernel with $\nu = 1.5$, combined with a constant kernel and a white-noise kernel, was used to account for nonlinear relationships and measurement noise. The model parameters were optimized using 50 optimizer restarts, and the target values were normalized before training.

The GPR model produced both a predicted crack position and an associated uncertainty estimate. A 95% prediction interval could therefore be calculated from the predicted mean and standard deviation. However, the calibration of this interval was not separately validated in the present study. The localization task was limited to estimating the x-coordinate of Crack 1.

Cracks 2 and 3, crack depth, severity, and the y-coordinate were not included in the prediction task.

To demonstrate the possible use of the classifier in health monitoring, the trained SVM was applied to a simulated sequence containing 10 healthy samples followed by 15 cracked samples. A damage index was calculated using the probability of the health class:

$$DI(t) = 1 - P_{SVM}(healthy|X(t)) \qquad 10$$

An alarm threshold of $DI = 0.5$was used. This demonstration involved repeated application of the trained SVM to individual samples and did not include temporal filtering, recursive estimation, or a separate sequential-learning model. PCA was used only to visualize the feature distribution and was not included in the classification or regression process.

6. Results and Discussion

A. FEM and Piezoelectric Response

The FEM results show the mechanical and electrical response of the aluminium beam with the attached PZT patches. The stress, electric potential, and electric field plots confirm that the actuator produces a measurable electromechanical response in the beam.

The frequency-response curve between 50 and 350 Hz shows an increase in the electrical response as the frequency increases.

However, no clear resonance peak was observed within this range. This suggests that the dominant resonance may occur outside the selected frequency range.

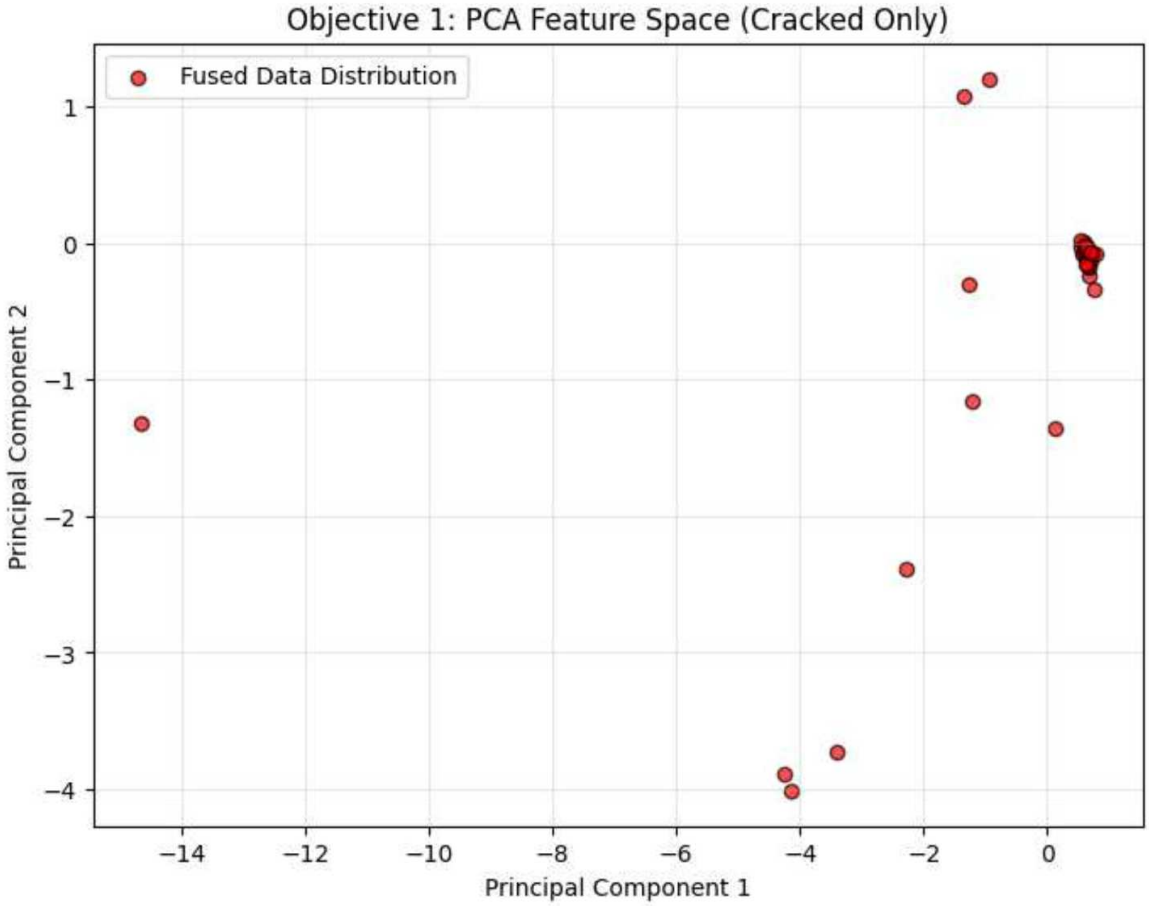
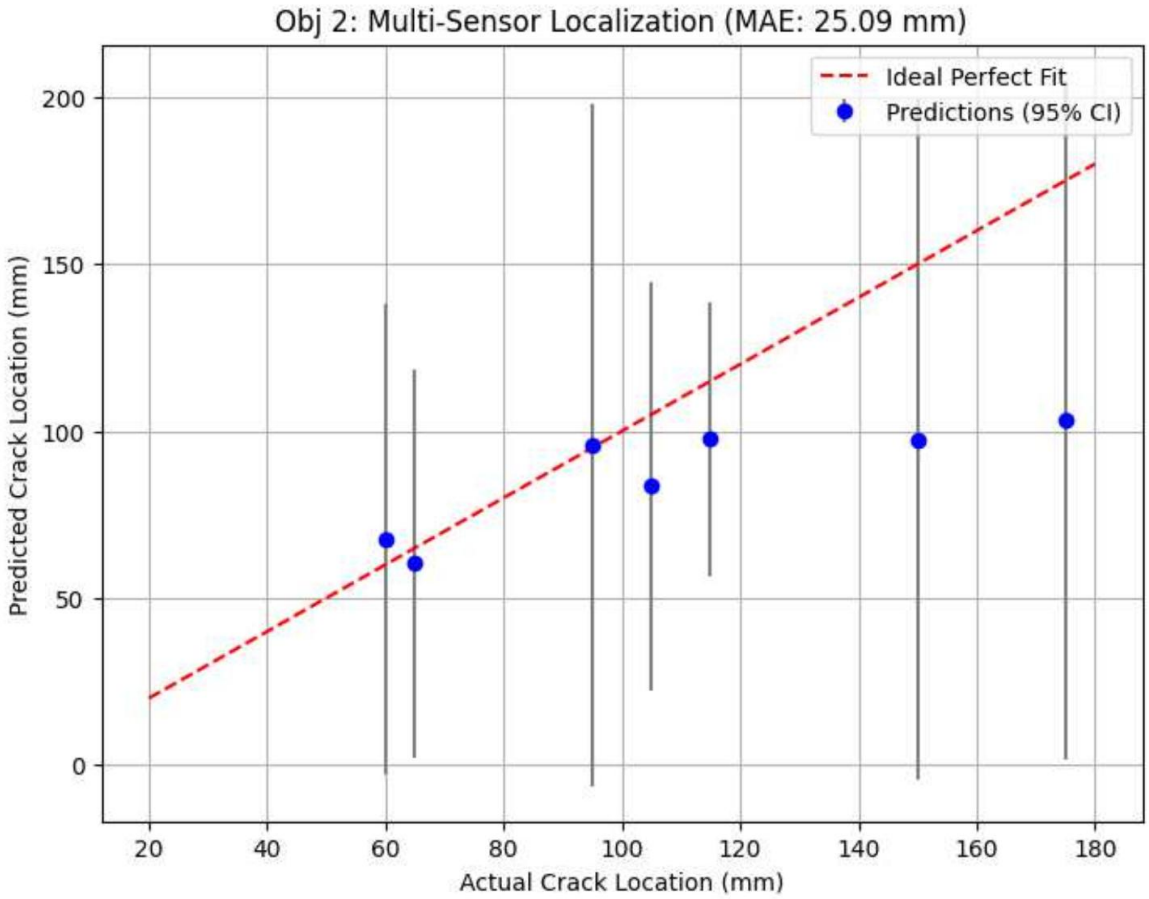


Figure 5 : PCA projection of the extracted features for cracked samples.

B. Feature Distribution

The PCA plot shows that most samples are grouped close to one another, while a few samples are located farther away from the main cluster. This indicates that the piezoelectric response changes for certain crack positions and that the extracted features capture variations in the simulated signals. Since the plot includes only cracked samples, it is used to show feature variation rather than direct separation between healthy and cracked conditions.

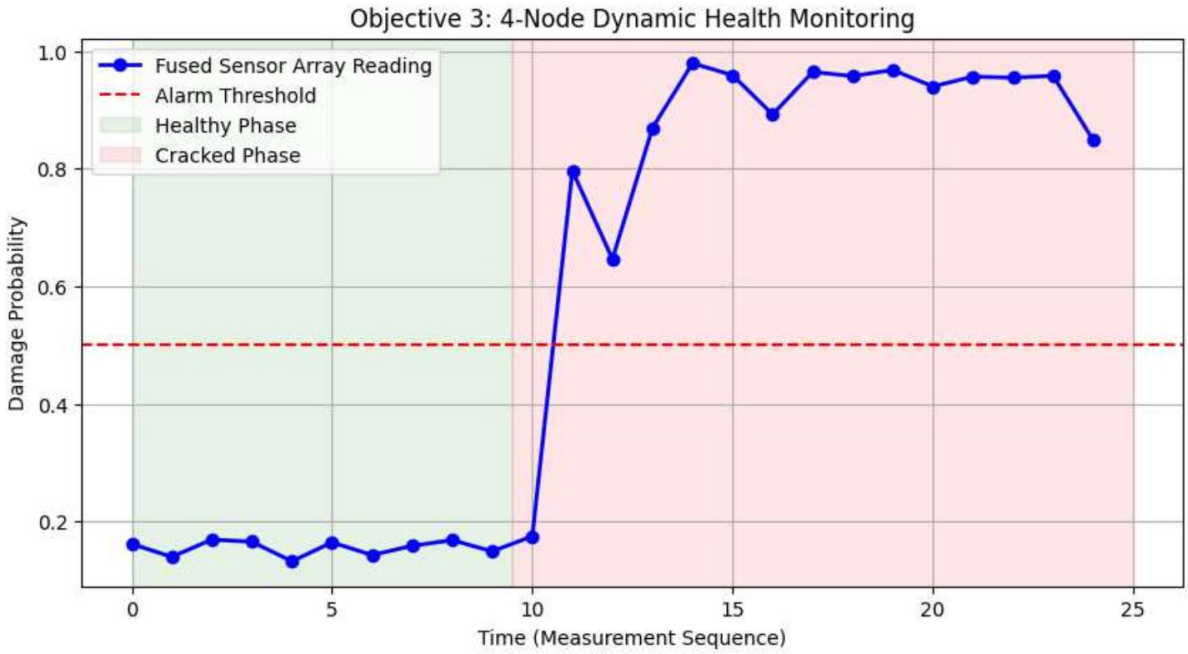


C. Crack Localization Results

Figure 6 : Actual and predicted crack positions obtained using GPR, with 95% predictive intervals.

The GPR model achieved a mean absolute error of **25.09 mm** when estimating the position of Crack 1. The predicted values follow the general trend of the actual crack positions, although some predictions show noticeable errors.

The wide confidence intervals for several points indicate that the model is uncertain about some of its predictions. Therefore, the results demonstrate the potential of the proposed approach for crack localization, but the current accuracy is still limited. A larger dataset and further validation would be needed to improve confidence in the predicted positions.



D. Dynamic Health-Monitoring Results

Figure 7 : Damage-index response during the simulated transition from healthy to cracked conditions.

During the healthy phase, the damage index remains below the alarm threshold of 0.5. Once the simulated cracked phase begins, the index increases sharply and remains above the threshold, with small variations between successive measurements.

This result shows that the trained classifier can identify the change from a healthy to a cracked condition under the simulated test conditions. However, the result is based on repeated predictions from the same SVM model and should be considered a demonstration rather than a complete real-time monitoring system.

E. Parametric and Robustness Analysis

The main parameter investigated in this study was the longitudinal position of Crack 1. Other parameters, such as crack depth, sensor and actuator placement, excitation frequency, number of measurement points, and noise level, were not systematically varied. Their effects on model performance remain to be investigated in future work.

7. Conclusion

This study explored the use of piezoelectric sensors and machine-learning techniques for crack detection and localization in an aluminum beam. The FEM results confirmed that the beam-PZT system produces measurable electrical responses that change with the presence and position of a crack.

The SVM classifier successfully demonstrated the ability to distinguish between healthy and cracked conditions in the simulated monitoring sequence. The GPR model also showed potential for estimating the longitudinal position of Crack 1, achieving a mean absolute error of 25.09 mm. However, the wide prediction intervals indicate that the localization results still involve considerable uncertainty.

Overall, the results show that combining FEM simulations with machine learning can provide a useful approach for structural health monitoring. However, the current study is limited by the small simulation dataset and the lack of experimental validation. Future work should focus on increasing the dataset size, testing different crack and sensor configurations, evaluating noise effects, and validating the models using experimental measurements.

References

[1] C. Sbarufatti, G. Manson, and K. Worden, A numerically-enhanced machine learning approach to damage diagnosis using a Lamb wave sensing network," Journal of Sound and Vibration, vol. 333, no. 19, pp. 4499–4525, May 2014, doi: 10.1016/j.jsv.2014.04.059.

[2] C. R. Farrar and K. Worden, An introduction to structural health monitoring," Philosophical Transactions of the Royal Society A Mathematical Physical and Engineering Sciences, vol. 365, no. 1851, pp. 303–315, Dec. 2006, doi: 10.1098/rsta.2006.1928.

[3] L. Colombo, M. D. Todd, C. Sbarufatti, and M. Giglio, On statistical Multi- Objective optimization of sensor networks and optimal detector derivation for structural health monitoring," Mechanical Systems and Signal Processing, vol. 167, p. 108528, Oct. 2021, doi: 10.1016/j.ymssp.2021.108528.

[4] D. Cusson, Z. Lounis, and L. Daigle, Durability Monitoring for Improved Service Life Predictions of Concrete Bridge Decks in Corrosive Environments," Computer-Aided Civil and Infrastructure Engineering, vol. 26, no. 7, pp. 524–541, Feb. 2011, doi: 10.1111/j.1467-8667.2010.00710.x.

[5] P. Hüthwohl and I. Brilakis, Detecting healthy concrete surfaces," Advanced Engineering Informatics, vol. 37, pp. 150–162, May 2018, doi: 10.1016/j.aei.2018.05.004.

[6] P. M. Ferreira, M. A. Machado, M. S. Carvalho, and C. Vidal, Embedded Sensors for Structural Health Monitoring: Methodologies and Applications Review," Sensors, vol. 22, no. 21, p. 8320, Oct. 2022, doi: 10.3390/s22218320.

[7] V. Kumar, T. Babu, B. Tiwari, and R. N. P. Choudhary, A review on PZT in civil engineering," Ferroelectrics, vol. 618, no. 1, pp. 186–199, Jan. 2024, doi: 10.1080/00150193.2023.2271325.

[8] C. Pitchford, B. L. Grisso, and D. J. Inman, Impedance-based structural health monitoring of wind turbine blades," Proceedings of SPIE, the International Society for Optical Engineering/Proceedings of SPIE, Apr. 2007, doi: 10.1117/12.715800.

[9] S. Bhattacharya, N. Yadav, A. Ahmad, F. Melands¯, and A. Habib, Multiple Damage Detection in PZT Sensor Using Dual Point Contact Method," Sensors, vol. 22, no. 23, p. 9161, Nov. 2022, doi: 10.3390/s22239161.

[10] E. García-Macías, L. Rodríguez-Tembleque, A. Sáez, and F. Ubertini, Crack detection and localization in RC beams through smart MWCNT/epoxy strip-like strain sensors,"Institutional Repository of the University of Granada (University of Granada), vol. 27, no. 11, p. 115022, Oct. 2018, doi: 10.1088/1361-665x/aae668.

[11] B. R. Seshadri and T. Krishnamurthy, Structural Health Management of Damaged Aircraft Structures Using Digital Twin Concept," NASA STI Repository (National Aeronautics and Space Administration), Jan. 2017, doi: 10.2514/6.2017- 1675.

[12] M. Torzoni, M. Tezzele, S. Mariani, A. Manzoni, and K. Willcox, A digital twin framework for civil engineering structures," Virtual Community of Pathological Anatomy (University of Castilla La Mancha), vol. 418, p. 116584, Nov. 2023, doi: 10.1016/j.cma.2023.116584.

[13] J. G. Greener, S. M. Kandathil, L. Moffat, and D. T. Jones, A guide to machine learning for biologists," Nature Reviews Molecular Cell Biology, vol. 23, no. 1, pp. 40–55, Sep. 2021, doi: 10.1038/s41580-021-00407-0.

[14] Mathematics for Machine Learning." doi: 10.1017/9781108679930.

[15] H. Tahraoui et al., Mixed coagulant-flocculant optimization for pharmaceutical effluent pretreatment using response surface methodology and Gaussian process regression," SPIRE - Sciences Po Institutional REpository, vol. 169, pp. 909–927, Nov. 2022, doi: 10.1016/j.psep.2022.11.045.

[16] A. Thelen, X. Huan, N. H. Paulson, S. Onori, Z. Hu, and C. Hu, Probabilistic machine learning for battery health diagnostics and prognostics—review and perspectives," npj Materials Sustainability, vol. 2, no. 1, Jun. 2024, doi: 10.1038/s44296-024-00011-1.

[17] Physics-informed machine learning for Structural Health Monitoring." doi: 10.48550/arxiv.2206.15303.

[18] E. J. Cross, S. J. Gibson, M. R. Jones, D. J. Pitchforth, S. Zhang, and T. J. Rogers, Physics-Informed Machine Learning for Structural Health Monitoring," in arXiv (Cornell University), Cornell University, 2021, pp. 347–367. doi: 10.1007/978- 3-030-81716-9_17.

[19] K. Kontolati, S. Goswami, G. E. Karniadakis, and M. D. Shields, Learning nonlinear operators in latent spaces for real-time predictions of complex dynamics in physical systems," Nature Communications, vol. 15, no. 1, p. 5101, Jun. 2024, doi: 10.1038/s41467-024-49411w.

[20] M. L. Palmeri, A. C. Sharma, R. R. Bouchard, R. W. Nightingale, and K. R. Nightingale, A finite-element method model of soft tissue response to impulsive acoustic radiation force," IEEE Transactions on Ultrasonics Ferroelectrics and Frequency Control, vol. 52, no. 10, pp. 1699–1712, Oct. 2005, doi: 10.1109/tuffc.2005.1561624.

[21] I. Garcia-Vargas, L. Barthe, P. Tierce, and O. Louisnard, Simulations of a full sonoreactor accounting for cavitation," Ultrasonics Sonochemistry, vol. 91, p. 106226, Nov. 2022, doi: 10.1016/j.ultsonch.2022.106226.

[22] T. Wang, B. Tan, M. Lu, Z. Zhang, and G. Lu, Piezoelectric Electro- Mechanical Impedance (EMI) Based Structural Crack Monitoring," Applied Sciences, vol. 10, no. 13, p. 4648, Jul. 2020, doi: 10.3390/app10134648.

[23] M. Ghazali and M. K. Mahdiabadi, High-precision multiple defect detection and localization in composite laminates using integrated piezoelectric sensing, regression and neural networks methods," Scientific Reports, vol. 15, no. 1, p. 35681, Oct. 2025, doi: 10.1038/s41598-025-19571-w.

[24] C. DomÌnguez-Monferrer, J. Fern·ndez-PÈrez, R. de A. Santos, M. H. Miguélez, and J. L. Cantero, Machine learning approach in non-intrusive monitoring of tool wear evolution in massive CFRP automatic drilling processes in the aircraft industry," e-Archivo (Carlos III University of Madrid), vol. 65, pp. 622–639, Oct. 2022, doi: 10.1016/j.jmsy.2022.10.018.

[25] S. Khalighi, T. Sousa, G. Pires, and U. Nunes, Automatic sleep staging: A computer assisted approach for optimal combination of features and polysomnographic channels," Expert Systems with Applications, vol. 40, no. 17, pp. 7046–7059, Jun. 2013, doi: 10.1016/j.eswa.2013.06.023.

[26] L. McManus, G. D. Vito, and M. M. Lowery, Analysis and Biophysics of Surface EMG for Physiotherapists and Kinesiologists: Toward a Common Language With Rehabilitation Engineers," Frontiers in Neurology, vol. 11, p. 576729, Oct. 2020, doi: 10.3389/fneur.2020.576729.

[27] J. Antoni and P. Borghesani, A statistical methodology for the design of condition indicators," UNSWorks (University of New South Wales, Sydney, Australia), vol. 114, pp. 290–327, May 2018, doi: 10.1016/j.ymssp.2018.05.012.

[28] A. Seely and P. T. Macklem, Complex systems and the technology of variability analysis," Critical Care, vol. 8, no. 6, Sep. 2004, doi: 10.1186/cc2948.

[29] L. Yu and V. Giurgiutiu, In-situ optimized PWAS phased arrays for Lamb wave structural health monitoring," Journal of mechanics of materials and structures, vol. 2, no. 3, pp. 459–487, May 2007, doi: 10.2140/jomms.2007.2.459.

[30] J. Yoon, J. Lee, G. Kim, S. Ryu, and J. Park, Deep neural network-based structural health monitoring technique for real-time crack detection and localization using strain gauge

sensors," Scientific Reports, vol. 12, no. 1, p. 20204, Nov. 2022, doi: 10.1038/s41598-022-24269-4.

[31] T. Ritto and F. A. Rochinha, Digital twin, physics-based model, and machine learning applied to damage detection in structures," arXiv (Cornell University), vol. 155, p. 107614, Jan. 2021, doi: 10.1016/j.ymssp.2021.107614.

[32] D. A. Gaul et al., Highly-accurate metabolomic detection of early-stage ovarian cancer," Scientific Reports, vol. 5, no. 1, p. 16351, Nov. 2015, doi: 10.1038/srep16351.

[33] A. Benjeddou, M. A. Trindade, and R. Ohayon, A Unified Beam Finite Element Model for Extension and Shear Piezoelectric Actuation Mechanisms," Journal of Intelligent Material Systems and Structures, vol. 8, no. 12, pp. 1012–1025, Dec. 1997, doi: 10.1177/1045389x9700801202.